

Super-ponderomotive electron spectra from efficient, high-intensity, kHz laser-water interactions

Scott Feister,^{1,2,*} Drake R. Austin,^{1,2,3} John T. Morrison,⁴ Kyle D. Frische,² Chris Orban,^{1,2} Gregory Ngirmang,^{1,2} Abraham Handler,^{1,3} Mark Schillaci,^{1,3} Enam A. Chowdhury,^{1,5} R.R. Freeman,¹ and W.M. Roquemore⁶

¹*Department of Physics, The Ohio State University, Columbus, OH, 43210, USA*

²*Innovative Scientific Solutions, Inc., Dayton, OH, 45459, USA*

³*University of Dayton Research Institute, Dayton, OH, 45469, USA*

⁴*Fellow, National Research Council, Washington D.C., 20001, USA*

⁵*Intense Energy Solutions, LLC., Plain City, OH, 43064, USA*

⁶*Air Force Research Laboratory, WPAFB, OH, 45433, USA*

(Dated: May 4, 2018)

Direct electron spectrum measurements show MeV energy electrons generated backward along the laser axis by a $\lambda = 780$ nm, 40 fs, 2.9 mJ short-pulse laser ($1.5 \cdot 10^{18}$ W/cm²). Electrons pass through a 3 mm hole in the center of the final off-axis paraboloid (OAP) and are characterized by a magnetic spectrometer. The charge collected at the OAP is hundreds of pC per pulse. A mechanism for this super-ponderomotive backward electron acceleration is discussed in the framework of 3D Particle-in-cell simulations.

OCIS codes: (020.2649) Strong field laser physics; (350.5610) Radiation; (000.2190) Experimental physics.

High intensity lasers ($> 10^{17}$ W/cm²) have enabled particle acceleration to high energies (keV to GeV) through a variety of methods and mechanisms, all of which exploit the large laser and plasma electric fields present during intense laser interactions with matter. Such laser sources are capable of accelerating electrons to GeV energies through direct laser-field and/or laser wake-field acceleration [1–3]. In addition, ultra-intense laser-plasma interaction can create bright X-ray sources from high harmonic generation, bremsstrahlung collisions of electrons, betatron oscillations [4], and other techniques.

Laser acceleration of electrons to a relativistic energy of order 1 MeV with mJ-class tabletop short-pulse lasers could enable a high repetition rate (up to 1 kHz), compact, ultra-short (<100 fs) relativistic electron source. A source of this type could be particularly attractive as a seed for free electron lasers [5], which currently use short pulse laser generated photo-electrons as seed. Prior experiments in laser-based electron acceleration to \lesssim MeV energies have noted that acceleration mechanisms relying on the p -polarization of the laser can be enhanced through the presence of a laser pre-pulse [6]. The pre-pulse serves to create an expanding plasma in front of the target and the presence of this plasma allows for a rich variety of laser-plasma interactions that would not occur with a sharp vacuum-solid interface [7]. Experiments at these lower energies have noted that super-ponderomotive acceleration along the direction of the laser of up to 0.8 MeV is possible through oblique incidence, p -polarized interactions. Mordovanakis *et al.*[6] used a 3 mJ laser to accelerate 7 pC of charge with an energy spectrum peaked at 0.8 MeV, and Mao *et al.*[8]

used a 240 mJ laser to accelerate 100 pC of electrons per shot with similar energy. The mechanism that underlies this super-ponderomotive generation of electrons depends sensitively on the p -polarization of the incoming laser pulse and works best at large angles of incidence; in these experimental cases, $\geq 45^\circ$.

Unlike the aforementioned studies of electron acceleration backward at large angles relative to the laser, in this letter, we describe a direct measurement of super-ponderomotive electrons with an apparent 1.3 MeV peak energy and several hundred pC of charge accelerated anti-parallel to the laser, generated from a 2.9 mJ laser focused onto a water jet. This represents a vast improvement in efficiency over previously reported electron acceleration measurements with mJ-class lasers interacting with high density targets. Previously-identified mechanisms relying on p -polarization cannot explain our results obtained at near normal incidence. In a previous paper [9], we provided strong circumstantial evidence for the existence of high energy electrons accelerated backward along the laser axis, but no direct electron measurements were presented. In the current work, we present multiple direct electron spectra alongside accelerated charge and laser pre-pulse measurements, and compare these spectra with 3D Particle-in-cell (PIC) simulations.

The laser used for this experiment is a modified Red Dragon Laser (KM Labs). This multi-pass 1 kHz Ti:sapphire system delivers 4.8 mJ (2.9 mJ on target) with a pulse duration of 40 fs full-width at half-maximum (FWHM). The fully-amplified laser has a center wavelength of 780 nm and a bandwidth of 40 nm. To enable intensity scans, the laser energy is reduced by a factor of five to ten without changes to the beam amplification profile by use of a waveplate and polarizer located after the final amplifier (i.e. before the laser compressor).

* feister.7@osu.edu

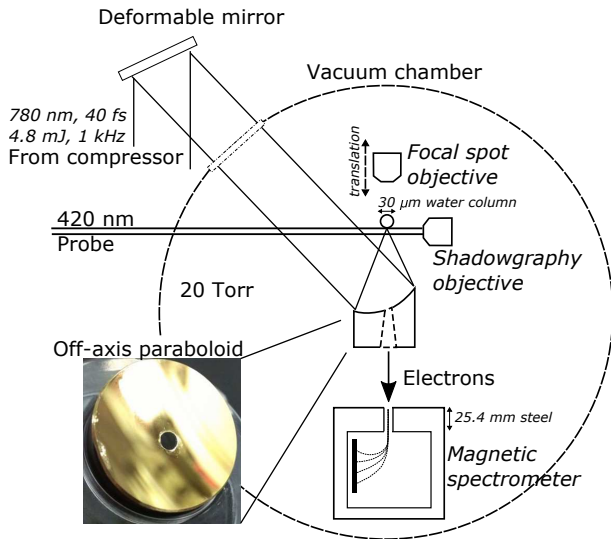


FIG. 1. To measure the electron spectrum in the direction anti-parallel to the laser axis (back-reflection direction), a 3 mm hole was drilled into the 25.4 mm diameter 30° gold-coated f/1.1 OAP. Electrons produced by intense laser interactions with a flowing water target pass through the hole in a 6.3° full-angle cone. Electron energies are characterized by a magnetic spectrometer located 127 mm behind the target. A wire is connected to the back of the electrically isolated aluminum-substrate OAP to use it as a Faraday cup, allowing for a measurement of electron number per pulse. The laser is polarized in the plane of the diagram.

The laser is focused with a 25.4 mm diameter, gold-coated 30° off-axis paraboloid (OAP) onto a streaming water jet target; the target area is sketched in Fig. 1. The water jet target is formed by pressurized flow through a 25 μm inner-diameter glass capillary nozzle. The water column is hydrodynamically stable and flows for about 2 mm before breaking up into droplets. For best flow stability, syringe pump pressure is chosen daily in a range between 350 PSI and 800 PSI. The resulting flow rate between 9 m/s and 14 m/s ensures a fresh target for each laser shot. A 20 Torr background pressure is maintained as the lowest operating pressure at which the water target does not freeze. The laser pointing stability in vacuum is $\sim 1 \mu\text{m}$. We aligned the laser focus to the water as follows: the water column is vertically translated such that the laser is incident 1 mm below the nozzle output, vertically angled for normal incidence (as seen in shadowgraphy, through air breakdown by the laser above 150 Torr), horizontally translated for near-normal incidence (as seen in back-reflection), and focally translated for strongest backward-going electron signal on the electron spectrometer. Because the laser interacts at normal incidence, reflections from the target have the potential to propagate backwards and damage the laser amplifiers. A large-aperture Pockels cell installed between the last amplifier and the compressor ensures rejection of 99% of backward-going light.

A hole is drilled in the OAP to allow electrons accel-

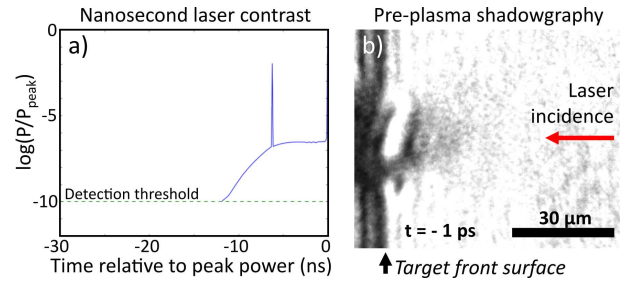


FIG. 2. a) The laser's nanosecond pre-pulse profile consists of a slowly-varying component (amplified spontaneous emission (ASE)) extending from -10 ns to 0 ns and a short pulse component positioned at -6.2 ns. This profile is calculated from measurements using multiple filterings on a Thorlabs DET10A Si-biased diode detector. Short pulse pre-pulse intensities are calculated by deconvolving the diode impulse response as in [9]. b) Shadowgraphy using a 420 nm, ~ 100 fs probe beam shows a snapshot of pre-plasma expansion 1 ps prior to the arrival of the main laser pulse.

erated anti-parallel to the laser to pass, enabling a direct spectral measurement of these electrons. The hole is 3 mm in diameter at the front, ensuring an unobstructed path to the spectrometer for any electrons ejected in a 6.3° full-angle cone from the target. The mount that holds the parabola is also modified to ensure clear paths to the spectrometer. If uncorrected, wavefront distortions due to the hole and associated surface deformations from the drilling process result in about a factor of five decrease in focal intensity. To correct this problem, a deformable mirror is inserted at the final section of the laser system and the focal plane intensity is optimized using a custom genetic algorithm.

The focal spot is measured using the focal spot objective (cf. Fig. 1) with the laser fully amplified. For this measurement, neutral density (ND) filters are inserted prior to the laser compressor, the water target is removed, and the vacuum chamber is held at atmospheric pressure. This setup results in a 2.2 μm FWHM focal spot on target, with 2 mJ contained in the laser focus. This is equivalent to the 2.2 μm FWHM focal spot measured before adding the OAP hole and deformable mirror.

A laser intensity of $1.5 \cdot 10^{18} \text{ W/cm}^2$ is calculated from the mean values of pulse duration, on-target energy in focus, and focal spot FWHM. These measurements occur at full laser amplification, but with added ND filtering, and without a target. Laser pulse duration is obtained through use of a single-shot autocorrelator [10] located after the laser compressor.

Laser temporal characteristics and pre-plasma evolution are quantified through three independent diagnostics. The laser's nanosecond pre-pulse profile (Fig. 2a) is measured by removing successive ND filters from a Thorlabs DET10A diode, then deconvolving the detector's impulse response to known short pulses [9]. This profile can be manipulated through adjustments to the timings and

alignments of four Pockels cells in the laser amplification chain. We note that a variety of nanosecond pre-pulse profiles can create a strong backward electron signal, but for the present work the nanosecond pre-pulse profile is a single femtosecond pre-pulse at -6.2 ns and about 10 ns of amplified spontaneous emission (ASE). Picosecond contrast is measured using a scanning third-order cross-correlator [11]; we did not observe any pre-pulses with intensity above 10^{13} W/cm². Shadowgraphy using a 420 nm probe beam laser (described in [12]) gives a time-resolved view of the pre-plasma expansion. As seen in Fig. 2b, the extent of pre-plasma 1 ps prior to the main pulse interaction is significant.

The charge per pulse ejected in the back-reflection direction is measured by using the OAP as a Faraday cup: the OAP is electrically isolated and the release of charge is analyzed over time. The Faraday cup current is alternatively analyzed in two ways: 1) by averaging the current over time using an electrometer, then dividing by the laser repetition rate, and 2) by integrating the voltage trace produced on a 100 MHz oscilloscope, and dividing by the termination resistance. Both methods agree within a factor of two, and the oscilloscope measurement is presented here. It is important to note that this charge per pulse is integrated over the entire 26° half-angle cone (less the hole) of electron emission that strikes the OAP.

The electron spectrum is measured with a custom, high-acquisition-rate electron spectrometer aligned to measure electrons through the center of the OAP hole. The electron spectrometer is located 127 mm behind the target (100 mm behind the OAP). The spectrometer uses a slit followed by two yoked magnets to deflect electrons according to their energy onto a phosphor screen (Lanex regular) that is pasted directly upon a bare linear CCD chip (MighTex CCD camera, Toshiba 1304DG linear CCD) and made light-tight with a 25 μ m thick covering of aluminum. Before measurements, a separate permanent magnet is swung into place between the OAP and electron slit (magnetically but not physically blocking the electrons' paths) to check that recorded signal drops to zero. This ensures the measured signal is from electrons and not due to a background x-ray or optical signal. The spectrometer is triggered and acquires electron traces at \sim 100 Hz when not limited by exposure time.

Electron energy positions at the detector are calibrated using Hall probe magnetic field measurements combined with relativistic particle deflection calculations. The detector stack's energy sensitivity is calibrated in two steps. First, the energy deposition efficiency into Lanex and the CCD depletion region is obtained as a function of electron input energy through MCNP [13] particle scattering calculations incorporating the aluminum cover, Lanex and CCD. Second, the amount of light that reaches the CCD is determined from diffusion calculations performed on the light generated at different Lanex depths. The contribution from the photon and electron signals are

then combined. The resultant detection efficiency curve, which is consistent with previous Lanex calibration efforts at and beyond 2 MeV [14], is presented in Fig. 3b with a low energy cutoff at approximately 250 keV.

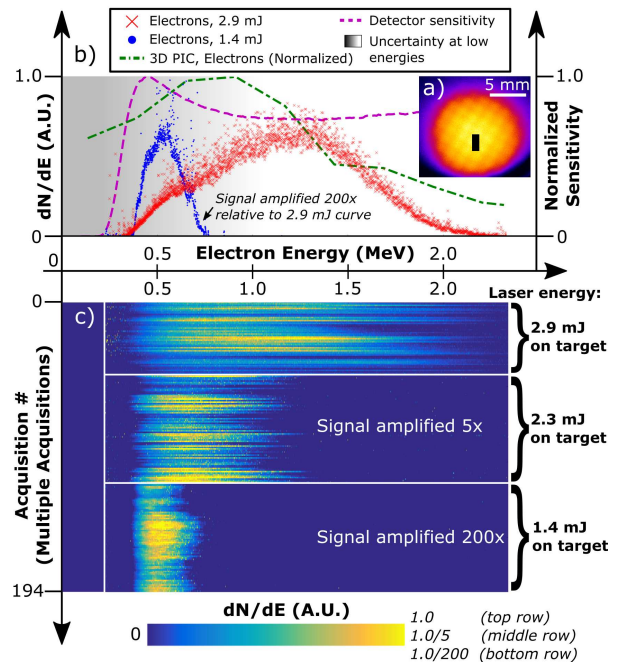


FIG. 3. a) The portion of the electron beam that passes through the hole of the OAP is imaged with a Lanex phosphor camera [15]. The black rectangle denotes the part of the beam (1 mm x 3.2 mm) that enters the magnetic spectrometer's slit and is energy-resolved. In this image, a diagnostic 250 μ m thick stainless steel mesh sits in front of the camera; both camera and mesh are removed before electron spectra measurements. b) In red crosses is an electron spectrum (10 ms CCD exposure) adjusted for energy bin size and detector sensitivity (maroon dashed line, right vertical axis). In blue dots is a measured spectrum for which the laser energy has been halved. The lower-energy end of the spectrum may be modified by spurious effects such as scattering along the beam path, and so this region is shaded. A spectrum of backward-ejected electrons from a 3D Particle-in-cell simulation is also shown. c) 194 consecutive spectral acquisitions are displayed. Each horizontal streak represents the spectrum from a single CCD exposure (10 ms for 2.9 mJ and 2.3 mJ laser energies, 100 ms for 1.4 mJ).

The results of our experiments are shown on Fig. 3. There are several important features of this result that require explanation. One result is that when the laser energy is reduced to below 1.4 mJ, the electron spectrum is confined to low energies; when the intensity increases to above 2.3 mJ, the spectrum shows much higher energy electrons. Further, as indicated by the change in signal, the total number of electron emitted increases dramatically. This increase in total yield is consistent with the total charge emitted measurements discussed above.

A 3D Particle-in-cell (PIC) simulation of the femtosecond timescale laser-matter interactions was performed

using the code LSP [16]. The laser parameters were similar to that of the highest energy experimental results shown. The cell size for these simulations was $\lambda/8 = 100$ nm and the electron density profile was assumed to be exponential with a $1.5 \mu\text{m}$ scale length. Backward-going electron spectra were obtained by tracking electron macroparticles and binning the charges and energies of these particles exiting the simulation. We find a large number of electrons accelerated to MeV energies in the back-reflection direction. Significant MeV electrons are present even for exponential scale lengths within a factor of two of the fiducial $1.5 \mu\text{m}$ scale length.

Fig. 3b shows 3D PIC simulation results for electrons ejected into the solid angle of the OAP hole. There are some similarities and some differences between the simulated and measured electron energy distributions. At the very lowest energies shown the experimental data shows a hard cut off for any laser intensity for electrons below approximately 350 keV. This is largely due to the detector sensitivity and does not appear to be a genuine indication that very few electrons are ejected at those energies. At somewhat higher energies, it is presently unclear whether the experimentally observed peak in energy for each intensity is due to the intrinsic nature of the source or whether moderately-energetic electrons ($\lesssim 1$ MeV) are being deflected out of the acceptance angle of the electron spectrometer. Geant4 [17] Monte-Carlo simulations indicate that the 20 Torr ambient pressure in the target chamber should divert $\sim 22\%$ of ~ 1 MeV electrons and 42% of 500 keV electrons from entering the spectrometer. The Geant4 simulations neglected the electrostatic repulsion of electrons en-route to the spectrometer, but this too should also play a significant role. Because these effects have not been compensated for in either the experimental or the 3D PIC results, the region below ~ 1 MeV has been shaded grey to highlight the challenge of interpreting the spectrum here.

In spite of the caveats just outlined, the measured spectra of Fig. 3 clearly shows electron acceleration to >1 MeV for a laser with an equivalent ponderomotive energy scale [18] of only ~ 90 keV. In the spectrum of Fig. 3b, electrons were measured backward along the laser axis with an apparent peak number density at 1.3 MeV. To our knowledge this kind of super-ponderomotive electron acceleration in the back-reflection direction has not been previously reported. We note that these spectra could only be obtained by the adjusting of nanosecond contrast parameters to give a pre-plasma of appropriate extent.

The electron number per pulse measured on the OAP/Faraday cup and associated with these high energy

spectra is very large: 600 pC/pulse. This Faraday cup measurement is integrated over all energies, and over a 26° emission angle. However, we have previously shown [9] through the insertion of a glass slide filter that at least half of the charge per pulse exceeds ~ 120 keV. Given the 2.9 mJ of on-target laser energy, we have produced ≥ 100 pC/mJ in association with a MeV-peaked electron spectrum; a surprisingly large charge per laser mJ when compared with measurements of electrons at oblique angles (e.g., 2.3 pC/mJ reported in [6], 0.4 pC/mJ in [8], and 0.15 pC/mJ in [19], albeit all with significantly smaller solid-angle electron beams). The LSP simulation predicts 100 pC of >150 keV electrons to be measured in the solid angle of our Faraday cup, which is within a factor of three of the experimental value. When the laser energy is reduced, the electron spectrum peak is significantly lower and the total signal is drastically reduced. This shift is highlighted in Figs. 3b and 3c. Given an energy reduction from 2.9 mJ on-target to 1.4 mJ on-target, the peak of the electron energy spectrum shifted down from 1.3 MeV to 500 keV.

A theoretical basis for the strong backward-going electron acceleration for this experiment is described in Orban *et al.*[15]. A standing wave is established between the forward-going laser and its backward reflection, accelerating electrons in both the forward and backward directions as outlined in Kemp *et al.*[20]. The back-directed electrons can be directly accelerated by the reflected laser fields.

In conclusion, we have measured super-ponderomotive electron acceleration in the back-reflection direction from a normal incidence, ~ 3 mJ laser interaction with water. The spectrum shows a peak at 1.3 MeV and the energetically and spatially integrated backward accelerated charge is 600 pC/pulse. This represents a major advance for the field in two ways: 1) the direction of super-ponderomotive electrons, and 2) the number of super-ponderomotive electrons. The theoretical mechanism proposed to explain this high energy, high efficiency electron acceleration should be further investigated experimentally. Future work will involve the controlled injection of a nanosecond timescale pre-pulse, statistical analyses of electron beam fluctuations using single-shot acquisitions, and spatial optimization of the electron beam with adaptive optics.

This research was sponsored by the Quantum and Non-Equilibrium Processes Division of the Air Force Office of Scientific Research, under the management of Dr. Enrique Parra, Program Manager. Support was also provided by the DOD HPCMP Internship Program. ABW: 88ABW-2015-3607.

[1] X. Wang, R. Zgadzaj, N. Fazel, Z. Li, S. A. Yi, X. Zhang, W. Henderson, Y.-Y. Chang, R. Korzekwa, H.-E. Tsai, C.-H. Pai, H. Quevedo, G. Dyer, E. Gaul, M. Martinez,

A. C. Bernstein, T. Borger, M. Spinks, M. Donovan, V. Khudik, G. Shvets, T. Ditmire, and M. C. Downer, Nature Communications 4 (2013), 10.1038/ncomms2988.

- [2] S. Mangles, C. Murphy, Z. Najmudin, A. Thomas, J. Collier, A. Dangor, E. Divall, P. Foster, J. Gallacher, C. Hooker, *et al.*, *Nature* **431**, 535 (2004).
- [3] W. P. Leemans, A. J. Gonsalves, H.-S. Mao, K. Nakamura, C. Benedetti, C. B. Schroeder, C. Tóth, J. Daniels, D. E. Mittelberger, S. S. Bulanov, J.-L. Vay, C. G. R. Geddes, and E. Esarey, *Phys. Rev. Lett.* **113**, 245002 (2014).
- [4] S. Kneip, C. McGuffey, J. L. Martins, S. F. Martins, C. Bellei, V. Chvykov, F. Dollar, R. Fonseca, C. Huntington, G. Kalintchenko, A. Maksimchuk, S. P. D. Mangles, T. Matsuoka, S. R. Nagel, C. a. J. Palmer, J. Schreiber, K. T. Phuoc, A. G. R. Thomas, V. Yanovsky, L. O. Silva, K. Krushelnick, and Z. Najmudin, *Nature Physics* **6**, 980 (2010).
- [5] R. Akre, D. Dowell, P. Emma, J. Frisch, S. Gilevich, G. Hays, P. Hering, R. Iverson, C. Limborg-Deprey, H. Loos, A. Miahnahri, J. Schmerge, J. Turner, J. Welch, W. White, and J. Wu, *Phys. Rev. ST Accel. Beams* **11**, 030703 (2008).
- [6] A. G. Mordovanakis, J. Easter, N. Naumova, K. Popov, P.-E. Masson-Laborde, B. Hou, I. Sokolov, G. Mourou, I. V. Glazyrin, W. Rozmus, V. Bychenkov, J. Nees, and K. Krushelnick, *Phys. Rev. Lett.* **103**, 235001 (2009).
- [7] W. L. Kruer, *The physics of laser plasma interactions* (Reading, MA (US); Addison-Wesley Publishing Co., 1988).
- [8] J. Y. Mao, L. M. Chen, X. L. Ge, L. Zhang, W. C. Yan, D. Z. Li, G. Q. Liao, J. L. Ma, K. Huang, Y. T. Li, X. Lu, Q. L. Dong, Z. Y. Wei, Z. M. Sheng, and J. Zhang, *Phys. Rev. E* **85**, 025401 (2012).
- [9] J. T. Morrison, E. A. Chowdhury, K. D. Frische, S. Feister, V. M. Ovchinnikov, J. A. Nees, C. Orban, R. R. Freeman, and W. M. Roquemore, *Physics of Plasmas* (1994-present) **22**, 043101 (2015).
- [10] F. Salin, P. Georges, G. Roger, and A. Brun, *Appl. Opt.* **26**, 4528 (1987).
- [11] S. Luan, M. H. R. Hutchinson, R. A. Smith, and F. Zhou, *Measurement Science and Technology* **4**, 1426 (1993).
- [12] S. Feister, J. A. Nees, J. T. Morrison, K. D. Frische, C. Orban, E. A. Chowdhury, and W. M. Roquemore, *Review of Scientific Instruments* **85**, 11 (2014).
- [13] R. Forster, L. J. Cox, R. F. Barrett, T. E. Booth, J. F. Briesmeister, F. B. Brown, J. S. Bull, G. C. Geisler, J. T. Goorley, R. D. Mosteller, S. E. Post, R. E. Prael, E. C. Selcow, and A. Sood, *Nucl. Instrum. Meth. B* **213**, 82 (2004), 5th Topical Meeting on Industrial Radiation and Radioisotope Measurement Applications.
- [14] Y. Glinec, J. Faure, A. Guemnie-Tafo, V. Malka, H. Monard, J. P. L. Larbre, V. De Waele, J. L. Marignier, and M. Mostafavi, *Review of Scientific Instruments* **77**, 103301 (2006).
- [15] C. Orban, J. T. Morrison, E. A. Chowdhury, J. A. Nees, K. Frische, S. Feister, and W. M. Roquemore, *Physics of Plasmas* (1994-present) **22**, 023110 (2015).
- [16] D. Welch, D. Rose, R. Clark, T. Genoni, and T. Hughes, *Computer Physics Communications* **164**, 183 (2004).
- [17] S. Agostinelli, J. Allison, K. Amako, J. Apostolakis, H. Araujo, P. Arce, M. Asai, D. Axen, S. Banerjee, G. Barrand, *et al.*, *Nucl. Instrum. Meth. A* **506**, 250 (2003).
- [18] S. C. Wilks, W. L. Kruer, M. Tabak, and A. B. Langdon, *Phys. Rev. Lett.* **69**, 1383 (1992).
- [19] J. Uhlig, C.-G. Wahlström, M. Walczak, V. Sundström, and W. Fullagar, *Laser and Particle Beams-Pulse Power and High Energy Densities* **29**, 415 (2011).
- [20] A. J. Kemp, Y. Sentoku, and M. Tabak, *Phys. Rev. E* **79**, 066406 (2009).